Shear Behavior of Circular Concrete Members Reinforced with GFRP Bars and Spirals at Shear Span-to-Depth Ratios between 1.5 and 3.0

Ahmed H. Ali[1]; Hamdy M. Mohamed[2]; and Brahim Benmokrane[3]

Abstract: In the last decade, the shear strength of concrete members with rectangular cross sections reinforced with fiber-reinforced polymers (FRPs) has received considerable attention. Yet no research seems to have investigated circular concrete members reinforced with FRP reinforcement under shear loads. This paper presents the results of an investigation of the shear strength and behavior of six circular concrete specimens reinforced with glass-FRP (GFRP) bars and spirals. The specimens, which measured 3,000 mm in length by 500 mm in diameter, were tested under four-point bending. The test parameters included the shear span-to-depth ratio (a/d) ranging from 1.5 to 3.0 and the GFRP spiral reinforcement ratio with different spiral spacings (100, 150, and 200 mm) and spiral diameters (13 and 15 mm). As designed, the specimens failed in shear due to GFRP spiral rupture or flexural-shear failure for the specimens with $a/d > 2.5$ and strut crushing combined with spiral rupture for the specimens with $a/d < 2.5$. The experimental results were compared to the current sectional models and the strut-and-tie model in codes and design guidelines as well as to the available analytical approach, which is based on the modified compression field theory. The comparison indicates that the shear capacity of FRP-reinforced concrete members with circular cross sections may be determined with the shear design provisions developed for rectangular sections within a variable degree of conservativeness. **DOI: 10.1061/(ASCE)CC.1943-5614.0000707.** © *2016 American Society of Civil Engineers.*

Author keywords: Circular concrete members; Shear span-to-depth ratio; Shear; Fiber-reinforced polymer (FRP) bars and spirals.

Introduction

Circular reinforced concrete (RC) members are extensively used as piers and piles in bridges and as fender piling in marine environments because they are easy to build and provide equal strength in all directions under lateral loads. These members have limited service lives and high maintenance costs when used in harsh environments due to the corrosion of the steel reinforcement. In North America, it has been estimated that the repair and replacement of piling systems costs billions of dollars annually (Benmokrane et al. 2016; Mohamed et al. 2014). In the last decade, the use of fiber-reinforced polymer (FRP) as an alternative reinforcing material in RC structures has emerged as an innovative solution to the corrosion problem [ACI 440.1R-15 (ACI 2015)]. Today, glass-FRP (GFRP) bars are becoming more attractive to the construction industry because they cost less than other types of FRP materials. Moreover, the cost of GFRP bars has been dropping in recent years, primarily due to a larger market and greater competition. GFRP bars have been used successfully as the main reinforcement in concrete bridges, parking garages, tunnels, and soft-eyes (Nanni and Faza 2002; Mohamed and Benmokrane 2014). Therefore, the development of reinforced concrete with GFRP bars and their application in infrastructure is gaining considerable interest in the civil engineering community.

Extensive research programs have been conducted to investigate the shear behavior of concrete members reinforced with GFRP bars and stirrups with rectangular cross sections (Razaqpur and Spadea 2015; Alam and Hussein 2012; Bentz et al. 2010; Ahmed et al. 2010; Fico et al. 2008; El-Sayed and Benmokrane 2008; El-Sayed et al. 2006; Shehata et al. 2000; Alkhrdaji et al. 2001; Guadagnini et al. 2006; Tottori and Wakui 1993). These studies specifically have assessed and compared the shear strength predictions of FRP-RC specimens with rectangular sections based on various codes of practice. As a result, several guidelines and code standards have been published, including design equations for assessing total shear resistance (V_r): ACI 440.1R-15, CSA S806-12 (CSA 2012), CSA S6-14 (CSA 2014a), and the Japan Society of Civil Engineers (JSCE 1997). They all follow the traditional ($V_{cf} + V_{sf}$) philosophy but significantly differ in the manner in which they estimate the contributions of concrete (V_{cf}) and diagonal tension reinforcement (V_{sf}) to the V_r. Recently, Thomas and Ramadass (2015) proposed a model to assess the shear strength of FRP-RC beams. The proposed model accounts for the compressive strength of concrete, the bar modulus of elasticity, the longitudinal reinforcement ratio, the shear span-to-depth ratio, and the beam size effect. The proposed model provided conservative predictions. In contrast, studies on the shear behavior of circular concrete members that can be reinforced with GFRP bars and spirals have not yet been introduced. Moreover, none of the preceding FRP design standards have incorporated specific formulae for circular RC members. In general, FRP shear design provisions can be applied to circular members by using an equivalent rectangular cross section. The accuracy of such an approach should, however, be assessed

[1]Ph.D. Candidate, Dept. of Civil Engineering, Univ. of Sherbrooke, QC, Canada J1K 2R1. E-mail: Ahmed.Ali@usherbrooke.ca

[2]Postdoctoral Fellow, Dept. of Civil Engineering, Univ. of Sherbrooke, QC, Canada J1K 2R1; Assistant Professor, Helwan Univ., Egypt. E-mail: Hamdy.Mohamed@usherbrooke.ca

[3]Professor of Civil Engineering and Tier-1 Canada Research Chair in Advanced Composite Materials for Civil Structures and NSERC Chair in FRP Reinforcement for Concrete Structures, Dept. of Civil Engineering, Univ. of Sherbrooke, QC, Canada J1K 2R1 (corresponding author). E-mail: Brahim.Benmokrane@usherbrooke.ca

Note. This manuscript was submitted on November 20, 2015; approved on February 24, 2016; published online on May 17, 2016. Discussion period open until October 17, 2016; separate discussions must be submitted for individual papers. This paper is part of the ***Journal of Composites for Construction***, © ASCE, ISSN 1090-0268.

because circular GFRP spirals may not contribute to shear strength in the same way as rectangularly bent stirrups. That being said, limited research has been carried out during the last decade on the shear behavior of circular steel-reinforced concrete members (Jensen et al. 2010; Khalifa and Collins 1981; Clarke and Birjandi 1993; Priestley et al. 1994; Collins et al. 2008; Felthem 2004; Merta and Kolbitsch 2006; Turmo et al. 2009).

The calculation of the shear strength (V_{sf}) of FRP-RC members uses the same basic relationship as steel RC members, with the main difference being the tensile strength limitation of FRP stirrups versus steel stirrups. This limitation arises from the fact that bending FRP bars to form stirrups significantly reduces tensile strength at the bend location (Shehata et al. 2000; Ahmed et al. 2010). Recently, a number of studies have been carried out on the bend strength capacity of FRP stirrups using a B.5 test method [ACI 440.3R-04 (ACI 2004)], indicating that the tensile strength of the bent part of the FRP bar is significantly lower than that of the straight part (Ahmed et al. 2010; Ishihara et al. 1997). Nonetheless, the behavior or a standard test method for FRP spirals under tensile axial loading has not yet been reported.

In reinforced concrete members, the shear span-to-effective depth ratio (a/d) is sometimes less than 2.5 (deep beams) or greater than 2.5 (slender beams). There is a consensus that members with $a/d \geq 2.5$ resist the applied load primarily by beam action and that arch action makes an insignificant contribution to the strength and behavior of such beams. Sectional models are included in the codes and design guidelines to predict the shear strength of slender FRP-RC members. Appendix I presents a summary of these models for ACI 440.1R-15, CSA S806-12, CSA S6-14, and JSCE. Among these standards, CSA S806-12 provides a factor (k_a) to be multiplied by V_c to account for arch effect enhancing shear resistance. Moreover, valuable research has been conducted to investigate the effect of a/d on the behavior of FRP-RC beams (Alam and Hussein 2012; Sherwood and Noghreh Khaja 2012). In beams with low a/d values (less than 2.5), shear failure is governed by strut-and-tie behavior. Therefore, the strut-and-tie model (STM) will generate more accurate predictions of shear strength with failure governed by crushing of a diagonal strut (Kani et al. 1979; Collins et al. 2007, 2008). Strut-and-tie models are included in ACI 318-14 (ACI 2014) for steel reinforcement and in CSA S806-12 (CSA 2012) for FRP reinforcement using the same equations as CSA A23.3-14 (CSA 2014b), CSA S6-14 (CSA 2014a), and *AASHTO LRFD Bridge Design Specifications* (AASHTO 2012) for steel reinforcement. Appendix I shows the strut-and-tie design provisions according to CSA S806-12 (CSA 2012). Recently, these provisions were assessed to predict the shear strength of FRP-RC deep beams (Farghaly and Benmokrane 2014). The applicability of these provisions to FRP-RC members with circular sections and low a/d values needs to be investigated.

The following sections provide details of experimental work on the beam action versus the arch action of full-scale circular concrete members reinforced with GFRP bars and spirals tested under shear loading. A theoretical study was also conducted to verify the accuracy of the available design provisions in predicting the shear strength of specimens with a/d between 1.5 and 3.0.

Experimental Investigation

Material

GFRP bars and spirals were used to reinforce six circular concrete specimens in the longitudinal and transverse directions, respectively (Fig. 1). The GFRP longitudinal bars were pultruded while the transverse reinforcement was fabricated with a bending process

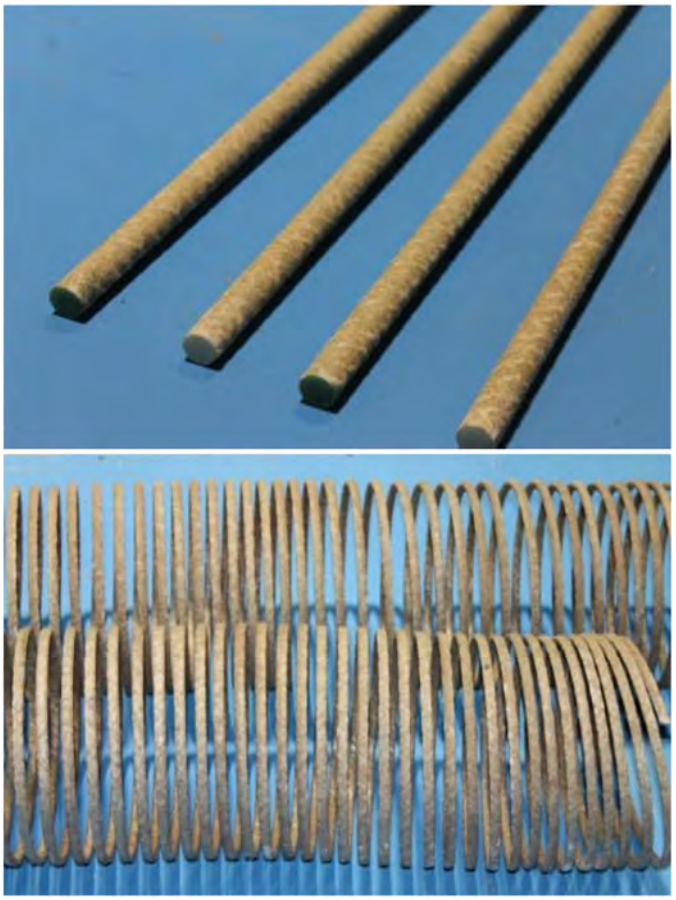

Fig. 1. GFRP bars and spirals

(BP Composites 2014). The reinforcement was made of continuous glass fiber rovings impregnated in a high-performance vinyl ester resin, additives, and fillers. The GFRP reinforcement had a sand-coated surface to enhance bond performance between the bars and the surrounding concrete. High-modulus (HM) GFRP bars [CSA S807-10 Grade III (CSA 2010)] with a bar size of #6 were used as a longitudinal reinforcement. Numbers 4 and 5 GFRP spirals were used as shear reinforcement. Table 1 provides the guaranteed properties of these bars and spirals as reported by the manufacturer. In addition, the bent tensile strength ($f_{fu,\text{bent}}$) of the #4 and #5 bars was calculated according to ACI 440.1R-15 and CSA S6-14 design equations for the bend strength of FRP bent bars. All beam specimens were cast on the same day with normal weight, ready-mixed concrete with an average compressive strength of 49.5 MPa. The actual compressive strength was determined based on the average test results of 10 concrete cylinders (150 × 300 mm) tested on the same day at the start of testing of the beam specimens.

Details of Test Specimens

A total of six full-scale circular RC specimens totally reinforced with GFRP bars and spirals were constructed and tested under monotonically increasing the shear load. The test matrix was arranged to assess the influence of the a/d and the GFRP spiral reinforcement ratio (spiral spacing and size) on the shear strength and behavior of circular concrete members. Each specimen was simply supported over a variable span and had a total length of 3,000 mm, an equivalent effective flexural depth (d) of 377 mm, an equivalent effective shear depth ($d_v = 0.9d$) of 340 mm, and a

Table 1. Mechanical Properties of the GFRP Bars and Spirals according to the Manufacturer

Barsize	Designated diameter (mm)	Nominal area (mm^2)	Area by immersion tests (mm^2)	Elastic tensile modulus (GPa)	Guaranteed tensile strength (MPa)
			GFRP bars		
#6	20	285	341	62.8	$f_{fu} = 1{,}103$
			GFRP spirals		
#4	13	127	135	47.0	$f_{ftu} = 1{,}050$ $f_{fu\,\text{bent}} = 615$[a] $f_{fu\,\text{bent}} = 1{,}019$[b] $f_{fu\,\text{bent}} = 765$[c]
#5	15	198	211	49.5	$f_{ftu} = 1{,}003$ $f_{fu\,\text{bent}} = 567$[a] $f_{fu\,\text{bent}} = 962$[b] $f_{fu\,\text{bent}} = 641$[c]

Note: f_{ftu} = guaranteed tensile strength of the straight portion of the bent bars; $f_{fu\,\text{bent}}$ = guaranteed tensile strength at the bent portion.
[a]Manufacturer according to ACI 440.1R-15 (B-5 test method).
[b]Manufacturer according to ACI 440.1R-15.
[c]Manufacturer according to CSA S6-14.

diameter of 500 mm. The equivalent effective depths were estimated based on the shear provisions (Clause 5.8.2.9) in the 2012 edition of the *AASHTO LRFD Bridge Design Specifications*. Table 2 provides the test matrix and reinforcement details of the beam specimens. Each specimen was identified with a code consisting of two letters (B and S) and two numbers. The letters B and S refer to beam specimen and spiral, respectively. The first number refers to the shear span-to-depth ratio of the test specimen (a/d between 1.5 and 3). The second number represents the spiral reinforcement ratio. As shown in Table 2, the effect of the GFRP spiral reinforcement ratio was investigated using #4 spirals at a spacing of 150 and 200 mm and using #5 spirals at a spacing of 150 mm. The effect of the a/d was investigated using four specimens with a/d equal to 1.5, 2.0, 2.6, and 3.0. These specimens were reinforced with 10 #6 GFRP bars and #4 GFRP spirals of 150 mm. Fig. 2 shows the dimensions, various configurations, and reinforcement details of the test specimens.

GFRP cages were assembled for the various beam configurations. The clear concrete cover was kept constant at 40 mm. The circular specimens were prepared for casting in very stiff Sonotube (Givesco, Montreal, Québec, Canada) concrete forms. Wooden plugs were used to seal the ends. The Sonotube concrete forms were placed in an inclined position and the concrete was cast from the top. External and internal vibration were used. Fig. 3 illustrates the fabrication process before and after casting.

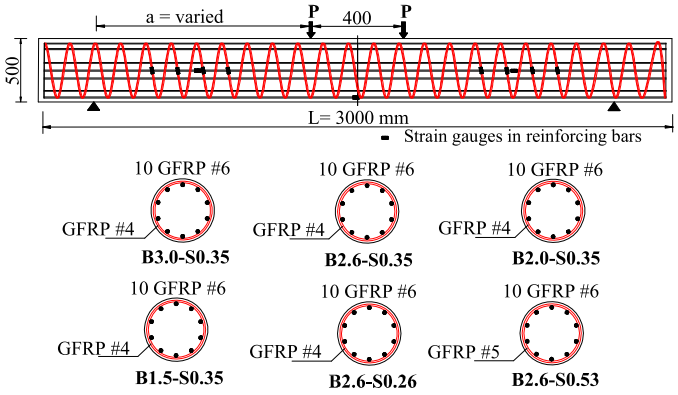

Fig. 2. Dimensions and reinforcement details of the tested circular specimens

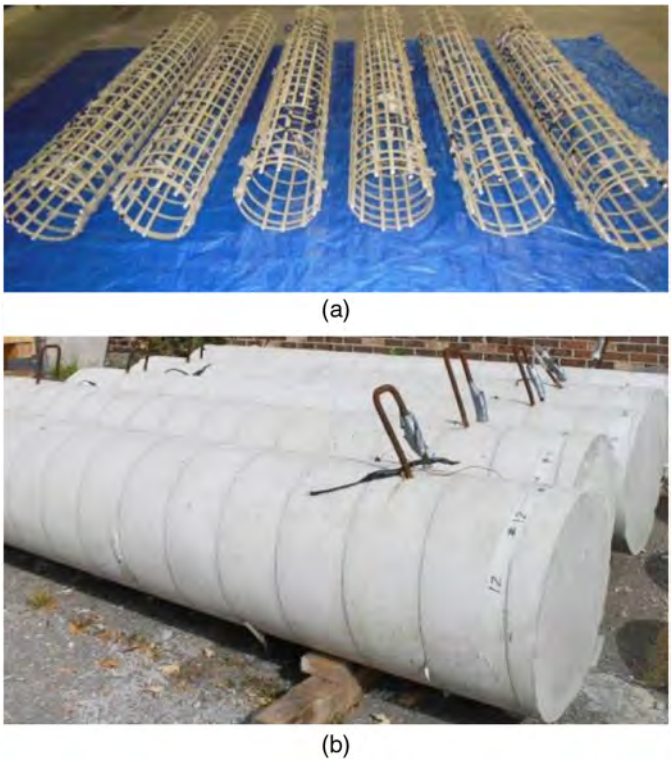

Fig. 3. Fabrication and preparation of the load beam specimens: (a) overview of the assembled GFRP cages; (b) circular beam specimens

Table 2. Details of Beam Specimens and Test Results

Beam identifier	Shear reinforcement			Ultimate shear $V_{u\,\text{exp}}$ (kN)	Load at failure (kN)	(θ°)	Stiffness (kN/mm)		Mode of failure
	a/d	Spiral	ρ_{fv} (%)				K_{cr}	K_u	
B3.0-S0.35	3.0	#4@150 mm	0.35	406	812	—	135.3	19.0	FS
B2.6-S0.35	2.6	#4@150 mm	0.35	419	837	46.5	138.1	24.2	GR
B2.0-S0.35	2.0	#4@150 mm	0.35	508	1,016	37.0	139.9	50.4	CS + GR
B1.5-S0.35	1.5	#4@150 mm	0.35	921	1,842	40.1	141.7	87.7	CS + GR
B2.6-S0.26	2.6	#4@200 mm	0.26	385	769	47.8	137.7	22.2	GR
B2.6-S0.53	2.6	#5@150 mm	0.53	503	1,005	59.6	139.5	25.5	GR

Note: CS = compression strut failure; FS = Flexural-shear failure; GR = GRFP spiral rupture; K_{cr} = initial stiffness; K_u = postcracking stiffness; $V_{u\,\text{exp}} = 0.5 \times$ failure load; θ° = angle of major shear crack.

Instrumentation and Test Setup

Strains in the longitudinal reinforcing bars and spirals were measured using electrical resistance strain gauges with gauge lengths of 6 mm. In addition, three strain gauges with a gauge length of 60 mm were mounted on the concrete top surface at three different levels (D, D/8, and D/4) at the midspan to measure compressive strains. Beam deflection was measured with linear variable differential transformer (LVDT) transducers placed at the midspan, under the point loads, and at the midshear span. Crack widths were monitored at each load increment by visual inspection using a hand-held micrometer with an accuracy of 0.01 mm. Fig. 4 presents a typical test arrangement, including the external instrumentation.

The test setup was designed and fabricated at the University of Sherbrooke's structural laboratory. The specimens were loaded under four-point bending as shown in Fig. 4. During the test, the load was monotonically applied at a stroke-controlled rate of 0.6 mm/min. An automatic data-acquisition system monitored by a computer was used to record the readings of the LVDTs, the load cells, and the strain gauges.

Experimental Results and Discussion

Table 2 provides a summary of the beam test results, including the failure load, ultimate shear load, initial and postcracking flexural stiffness, and modes of failure. It should be noted that each beam was symmetrically loaded with two concentrated loads and consequently, the failure load is the sum of the two concentrated loads. The following sections provide the test results, including the effect of the test parameters on the shear strength behavior of beam specimens.

Effect of Spiral Reinforcement Ratio on Load–Deflection Behavior

Fig. 5 shows the shear behavior of three circular RC specimens (B2.6-S0.26, B2.6-S0.35, and B2.6-S0.53) that were reinforced with different spiral reinforcement ratios (0.26, 0.35, and 0.53, respectively). These specimens had a constant shear span-to-depth ratio of 2.6. The spiral spacing (s) for these specimens was within the CSA S806-12 maximum spacing limit for transverse reinforcement ($0.6d_v \cot\theta$ or 400 mm), where d_v is the effective shear depth, taken as the greater of $0.9d$ (flexural depth) or $0.72h$ (overall thickness). In general, the behavior of these specimens can be divided into two stages. In the first stage, the "prior-to-flexural-cracking stage," all the specimens behaved similarly and approximately linearly. Specimen stiffness at this stage was almost identical regardless of spiral reinforcement ratio, representing the behavior of the uncracked specimen with the gross moment of inertia of the concrete cross section. After cracking, the beams behaved nearly linearly with reduced stiffness up to failure. This is attributed to the linear-elastic characteristics of the GFRP reinforcement. Specimen stiffness in this stage was insignificantly dependent on the spiral reinforcement ratio as well as the stiffness of the flexural reinforcement, which was constant for the three specimens. Fig. 5 and Table 2 indicate that the ultimate shear strength increased as the spiral reinforcement ratio increased. Increasing the shear reinforcement from 0.26 to 0.35 and 0.53 increased the shear capacity of the tested beams by 9 and 30.7%, respectively. Moreover, B2.6-S0.35 and B2.6-S0.53 evidenced enhanced stiffness when the major diagonal shear crack was compared to B2.6-S0.26, which had a lower shear reinforcement ratio. This can be attributed to the higher spiral reinforcement ratio that tends to control crack opening and propagation. Increasing the shear reinforcement ratio in B2.6-S0.35 and B2.6-S0.53 helped redistribute internal stresses, forming a truss action in which the reinforcement acts as tensile links and the concrete acts as compression diagonals.

Fig. 4. Test setup

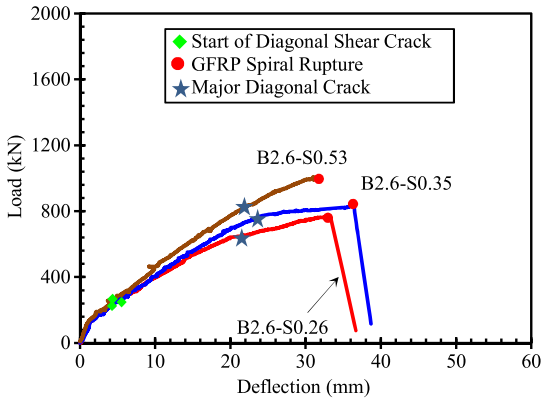

Fig. 5. Load–deflection response at midspan for the effect of the spiral reinforcement ratio

Effect of Shear Span-to-Depth Ratio on Load–Deflection Behavior

Fig. 6 shows the shear behavior of four circular RC specimens (B3.0-S0.35, B2.6-S0.35, B2.0-S0.35, and B1.5-S0.35) that were tested with different shear span-to-effective depth ratios (3.0, 2.6, 2.0, and 1.5, respectively). The figure shows that the a/d significantly influenced the load–deflection behavior. The figure indicates that the shear strength increased with reducing a/d from 3.0 to 2.0, then exhibited a considerable increment as the a/d reached 1.5. All specimens exhibited a nearly bilinear response up to failure except for the beam with the a/d of 1.5, which had nearly linear load–deflection behavior. The specimen with the a/d of less than 2.5

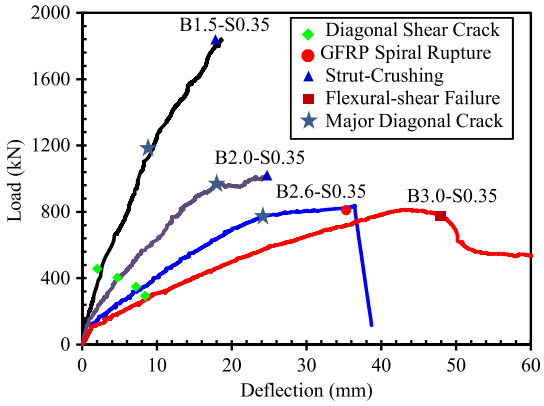

Fig. 6. Load–deflection response at midspan for the effect of the shear span-to-depth ratio

had no postpeak response because the failure was explosive. Evident in the figure is the initial stiffness (before cracking) and the postcracking flexural stiffness that were significantly affected when the a/d ratio decreased from 3.0 to 1.5. A noticeable enhancement in the initial stiffness was observed as the a/d decreased from 2.6 to 1.5, representing the shear behavior of the short beam. However, the initial stiffness of the beam with the a/d of 3.0 was similar to that of the beam with the a/d of 2.6, representing the shear behavior of the slender beam. On the other hand, decreasing the a/d from 3.0 to 2.0 gradually increased the postcracking flexural stiffness of the tested specimens then decreased the a/d from 2.0 to 1.5 and exhibited a remarkable steeper load–deflection response. This is evident since the flexural stiffness of B1.5-S0.35 ($k_u = 87.65$ kN/m) and B2-S0.35 ($k_u = 50.43$ kN/m) was approximately 3.6 and 2.0 times that of B2.6-S0.35 ($k_u = 24.24$ kN/m), respectively. This is attributed to the fact that, since the a/d was less than 2.5, their shear behavior and performance takes the shape of an arch action.

Crack Patterns and Modes of Failure

In this study, different failure modes associated with combined bending and shear were observed. Shear–compression failures (crushing of compression struts) accompanied by spiral rupture were observed for specimens of with span-to-depth ratios of 2 and 1.5, while diagonal shear failure accompanied by GFRP spiral rupture and flexural-shear failure were the dominant failure modes for specimens with span-to-depth ratios of 2.6 and 3, respectively. Fig. 7 provides the crack patterns and measured values of shear crack angles for each major crack in each specimen. In all the specimens, flexural cracks occurred first, irrespective of span-to-depth ratio or spiral spacing. As the load increased, additional vertical cracks appeared on the beam surface followed by the formation of diagonal cracks. A diagonal tension crack is generally defined as an inclined crack in the shear span that intersects the tensile reinforcement at an angle of approximately 45°. In the specimens with a/d equal to 3 and 2.6, these diagonal tension cracks generally originated as vertical flexural cracks that extended from the tensile side of the beam to slightly the top and then became inclined and progressed toward the loading point.

For the beam with $a/d = 3$, with increasing the load, more cracks appeared along the shear span. After a load level corresponding to approximately 72% of the failure load, no more cracks appeared, and only a widening of the existing cracks was observed. Although the shear span-to-depth ratio was 3, i.e., for this beam, the shear, and tensile stresses governed the cracking pattern. In this case, the flexural cracks under the loading point and the diagonal tension crack in the shear span simultaneously grew excessively wide. The final failure was found to depend on the widening of the diagonal cracks relative to that of the flexural cracks. The test was halted when one of the diagonal cracks near the loading point had opened significantly (Fig. 8), leading to excessive beam deformation and the GFRP tensile reinforcement reached a strain level of over 10,000 microstrains.

For a beam with a span-to-depth ratio of 2.6, the formation of diagonal cracks did not immediately lead to a final collapse. Instead, these cracks continued to develop with each increment of the applied load, and the ultimate loads sustained by the beam were, in general, considerably higher than the load at which the diagonal tension cracks first formed. The initial flexural cracks at the pure bending moment zone remained narrow throughout the tests. Failure occurred after the formation of two or more significant diagonal shear cracks near the midshear span that propagated through the compressive zone, leading to diagonal tension failure combined with the rupture of the GFRP spirals. Removing the concrete cover revealed the rupture of the GFRP spirals, with at least two of the GFRP spirals crossing a diagonal crack. The concrete cover under the layer of longitudinal reinforcement at the bottom of the beam was lost. The main difference in the final crack patterns of the three specimens ($a/d = 2.6$) was the number and spacing of the diagonal cracks that developed in the shear span: the higher the failure load, the greater the number of induced shear cracks. Fig. 9 shows the typical failure mode of the beam specimens with the a/d of 2.6. On the other hand, the two specimens with a/d less than 2.5 (2 and 1.5) exhibited major cracking that developed from the loading point to the support. Limited flexural cracks were observed. Diagonal tension cracks originated at about beam mid-depth and then progressed toward the nearer concentrated load and the supports. This eliminated the shear flow completely and the specimens had an arch action behavior. Because the arch action developed at an early loading stage, the initial cracks remained narrow throughout the tests. The number of vertical and inclined cracks was significantly lower for these specimens, however, due to arch action. At a load level of 45–55% of the failure load, a major diagonal crack formed, defining the concrete compression strut. Afterward, no more cracks developed and only widening of the former diagonal cracks could be observed. The crack progression in B1.5-S0.35 and B2.0-S0.35 supports the notion of the formation of a direct compressive-strut mechanism.

Fig. 10 shows the crack propagation and the final state of the shear–compression failure (crushing of the compression strut) accompanied by spiral rupture for the beam with the a/d of 2. In addition, Fig. 11 shows the crack propagation and final state of the strut-compression failure and rupture of a spiral in the beam with the a/d of 1.5. The failure crack extended diagonally from the load plate to the support plate. Failure of the two specimens was very brittle accompanied by an explosive sound. No premature failure due to anchorage failure of the tension reinforcement or due to bearing failure at the supports or at the loading points was observed. These figures show that the inclined crack pattern was more linear than curvilinear, as observed in the other specimens with span-to-depth ratios over 2. B1.5-S0.35 had only a single diagonal crack in each shear span.

Load-Flexural Tension Strain Relationship

Fig. 12 shows the measured applied load on the specimens versus the strain relationships for the GFRP longitudinal bars. In this figure, the strain was minimal until the concrete section cracked. The specimens exhibited similar strain behaviors up to this stage, except

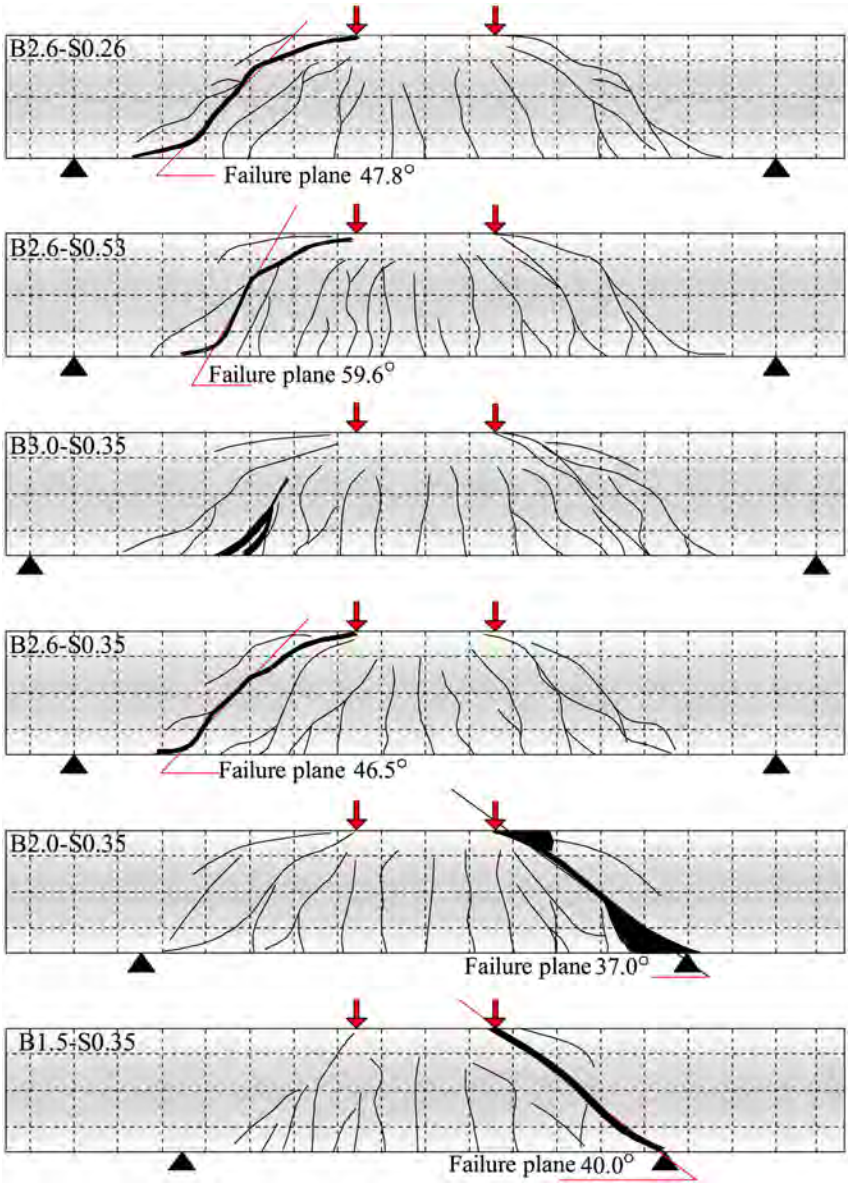

Fig. 7. Crack patterns of tested specimens

the specimens with $a/d \leq 2.5$. The figure indicates that the specimen with the higher shear span-to-depth ratio ($a/d = 3$) exhibited cracking at a lower load level (79 kN) compared to the other specimens. In contrast, the beam with the lowest a/d (1.5) evidenced a higher cracking load (approximately 187 kN). After cracking, the specimen with the lowest a/d (1.5) exhibited less bar strain than the specimens with the higher a/d (2.0, 2.6, and 3.0) at the same load level because the former had arch action, compared to the slender beam behavior of the latter. This can be attributed to the arch action for the beam with the a/d of 1.5, which is capable of transferring the load directly to the supports. After cracking, however, in the beam with the a/d of 3.0, the concrete stress was transferred to the reinforcement, which could result in a higher strain. The development of GFRP flexural strains in specimens with $a/d = 2.6$ was similar to the beam with $a/d = 2.0$. The maximum strains in the GFRP bars for specimens with a constant a/d (2.6) were approximately 8,130, 7,340, and 9,670 microstrains for B2.6-S0.26, B2.6-S0.35, and B2.6-S0.53, respectively. On the other hand, the measured strains in the GFRP bars for specimens with different shear span-to-depth ratios (3.0, 2.6, 2.0, and 1.5) were 11,800, 7,340, 6,737, and 10,969 microstrains, respectively. In general, this strain at the ultimate load shows that shear failure was not triggered by the GFRP bars rupturing.

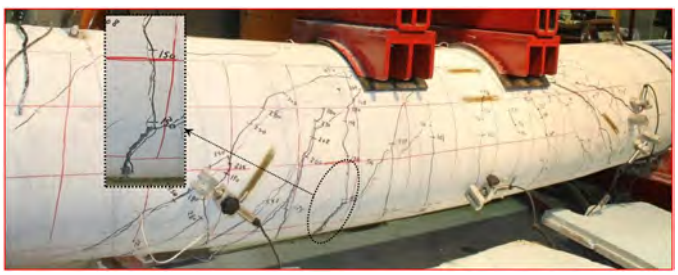

Fig. 8. Failure mode of specimen B3.0-S0.35 ($a/d = 3$)

Concrete Strains

Fig. 13 provides the measured compressive concrete strains at the midspan at three different levels from the top (D, D/8, and D/4).

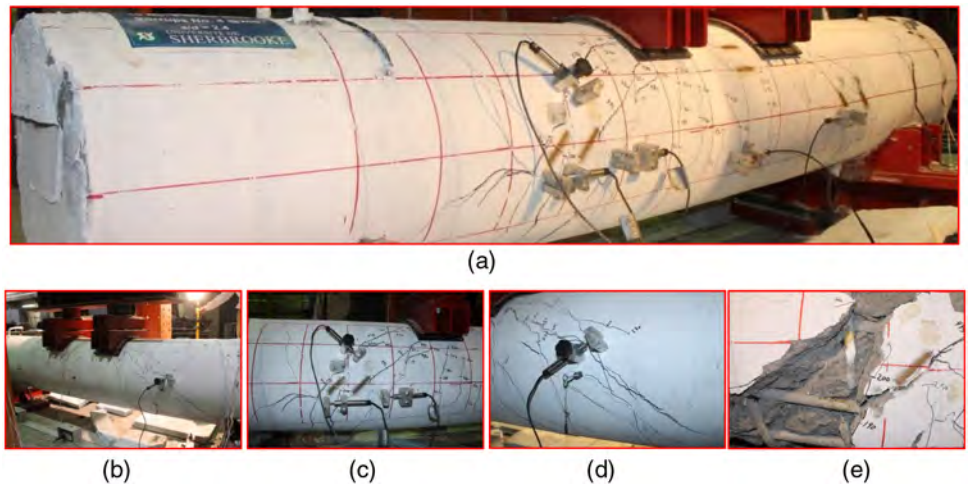

Fig. 9. Crack propagation and failure mechanism ($a/d = 2.6$): (a and b) crack pattern at a load level of 75% of failure, front and back view; (c and d) at a load level of 85%; (e) rupture of the GFRP spirals

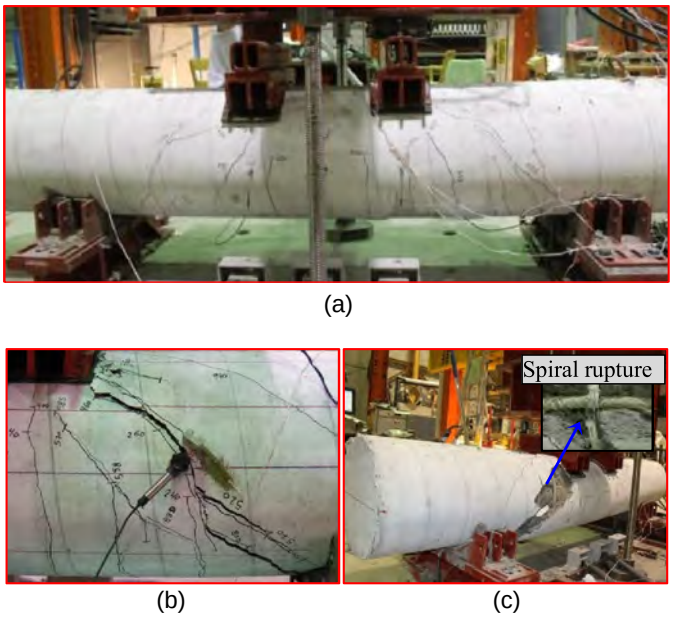

Fig. 10. Crack propagation and failure mechanism ($a/d = 2$): (a) crack pattern at a load level of 65% of failure; (b) crack pattern at a load level of 90% of failure; (c) crushing of the compression strut and spiral rupture

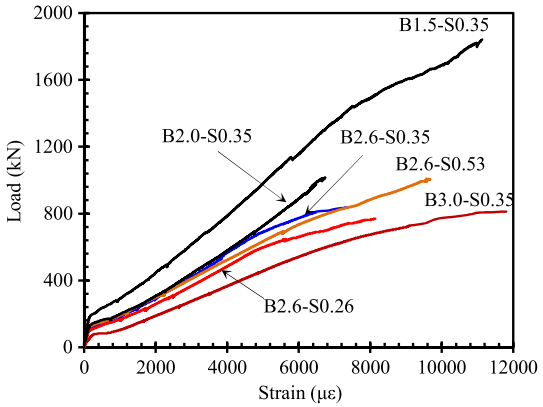

Fig. 12. Load–strain relationship for longitudinal reinforcement

The figure indicates that prior to cracking, the concrete strains were insignificant in all of the specimens and ranged from 110 to 200 microstrains. After cracking occurred, the strains differed almost linearly with increasing load up to failure. As shown in Fig. 13, the maximum recorded concrete strain before failure ranged from 2,840 to 3,800 microstrains. The higher strain was recorded for the specimen with the highest a/d (3.0). The recorded strains for B2.6-S0.26, B2.6-S0.35, and B2.6-S0.53 were similar and

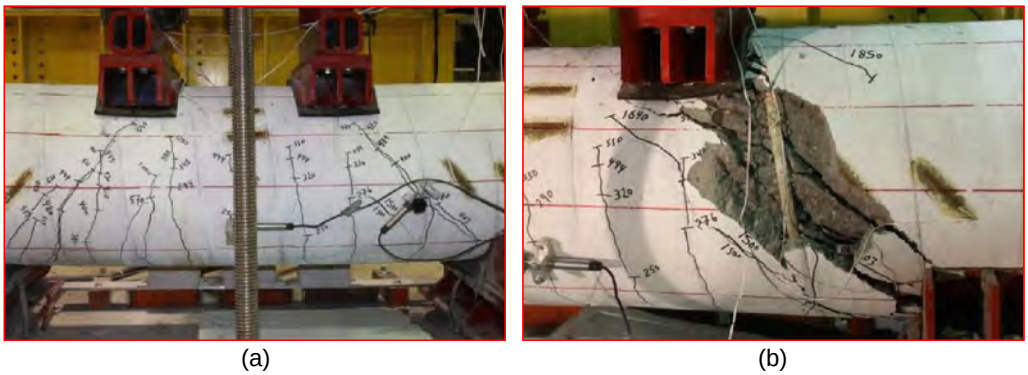

Fig. 11. Crack propagation and failure mechanism ($a/d = 1.5$): (a) crack pattern at a load level of 75% of failure; (b) crushing of compression strut and rupture of spiral

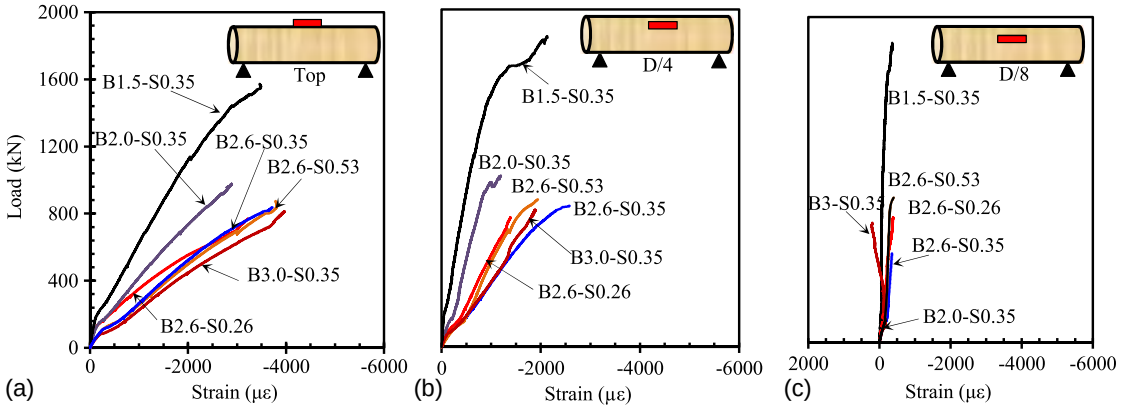

Fig. 13. Load–strain relationship for concrete: (a) at the top concrete surface; (b) at D/4; and (c) at D/8

approximately close to the limit of the concrete crushing strain of 3,500 microstrains specified in the CSA standards (CSA S806-12). The propagation of cracks at the shear span implies that the major diagonal tension–shear crack governed the failure mode of these specimens with no signs of crushing at the midspan. After cracking, the concrete beam with the lowest a/d (1.5) exhibited less concrete strain than the specimens with higher shear span-to-depth ratios (2.0, 2.6, and 3.0) at the same load level. Figs. 13(b and c) show the measured concrete strains at level D/8 and D/4 for all tested specimens. Fig. 13(b) shows that at all loading stages, the strain at level D/8 was less than that at level D, reaching no more than 2,600 microstrains. This indicates that the maximum strain was reached at the top surface of the beams. Fig. 13(c) also revealed that the strains at level D/4 were insignificant up to the ultimate failure load. This implies that the flexural cracks at the midspan did not penetrate into the compression zone.

Strain in GFRP Spirals

Spiral strains were measured using strain gauges attached to the GFRP spiral reinforcement at the midshear span. However, some of the strain data were unreliable because of the difficulties in measuring strains over the curved or twisted surface of the spirals. Besides, test observations revealed that the major diagonal crack did not always cross the spirals at the location of the strain gauges, which means that the effective strains measured in the spirals did not necessarily represent the maximum strain. Fig. 14 shows the applied load–spiral strain relationship. The figure indicates that prior to cracking, all the specimens showed the same behavior with insignificant spiral strain. Subsequent to diagonal shear cracking and with increasing loads, the spiral strain slowly and steadily increased. This indicates the transfer of internal forces from the concrete to the spirals. The figure indicates that in B1.5-S0.35, the GFRP spiral strain was activated at a higher load level than in the other specimens. This is attributed to the arch action in this beam, which delayed the load transfer to the GFRP spirals. After formation of the major diagonal cracking at a load level of 1,195 kN, however, the strain in the spiral for this beam increased progressively and recorded 3,135 microstrains before failure. On the other hand, the GFRP spiral in B2.6-S0.26 reached to the highest strain level (3,300 microstrains) compared to the other specimens.

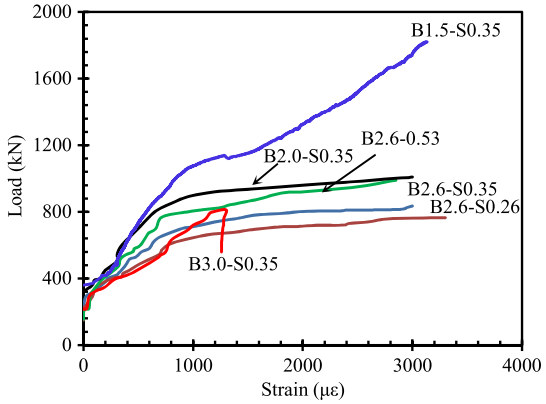

Fig. 14. Load–stirrup strain relationship at shear span

Effectiveness of GFRP Spirals

In this study, the effective stress of the GFRP spirals at failure (f_{fv}) of the test specimens was assessed based on the difference between the measured shear strength ($V_{\exp}$) and the shear force contributed by the concrete as measured at the initiation of the first diagonal shear crack (V_{cr}), which is reported in Appendix I. Based on the conventional truss model, the stress in the spirals at f_{fv} was determined as follows:

$$f_{fv} = \frac{(V_{\exp} - V_{cr})s}{\lambda_1 \lambda_2 A_{fv} d_v (\cot\theta + \cot\alpha)\sin\alpha} \tag{1}$$

where A_{fv} = area of the GFRP spiral; s = spiral spacing; d_v = effective shear depth of the beam; θ and α are, respectively, the angles of the observed diagonal shear cracks, or of the diagonal struts, and the inclination of the spiral to the beam axis (Felthem 2004) (Fig. 15); and λ_1 and λ_2 are two factors taking into account

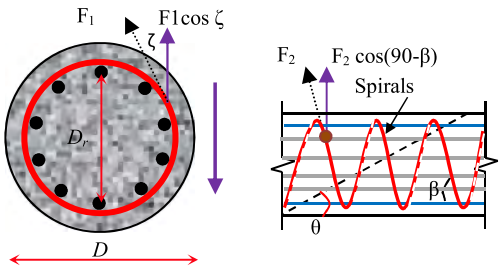

Fig. 15. Shear across a circular section

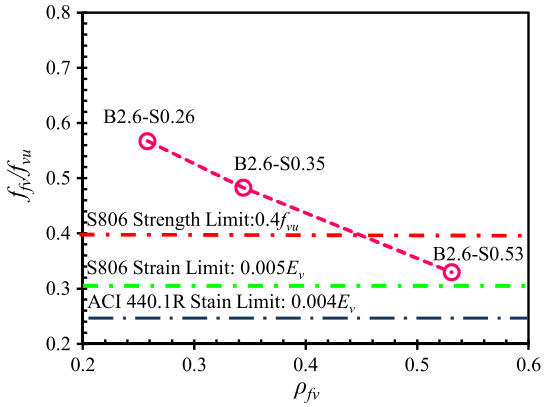

Fig. 16. Effect of shear reinforcement ratio on the effective capacity of the GFRP spirals

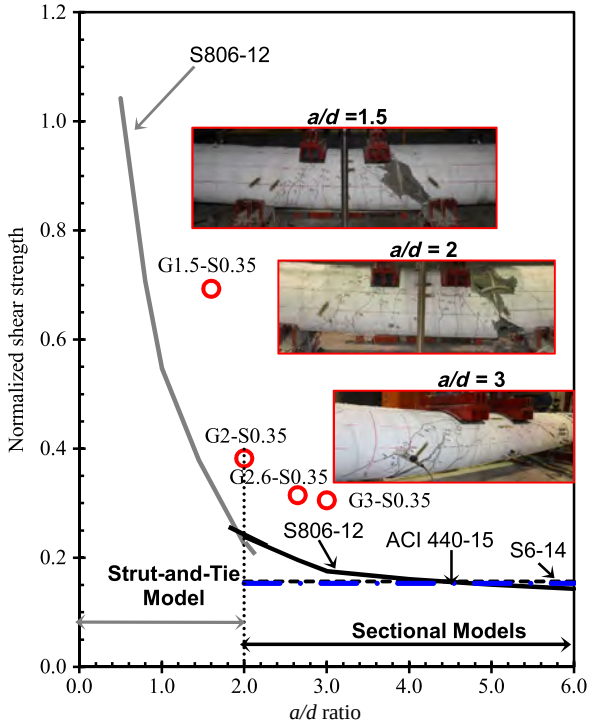

Fig. 17. Influence of a/d on shear strength

the effect of the spiral curvature (the inclination of the spiral with respect to the transverse axis) and the spiral inclination with respect to the longitudinal axis, respectively (Turmo et al. 2009; Clarke and Birjandi 1993). In the calculation, $\lambda_1 = 0.85$ and $\lambda_2 = 1.0$ were considered (Turmo et al. 2009).

Test results of shear strength for specimens with $a/d = 2.6$ were used to assess the contribution of the GFRP spiral because the failure of these specimens resulted from spiral rupture. Fig. 16 shows that f_{fv} at failure normalized to the tensile strength of the GFRP straight bar. The f_{fv} at failure ranged from 33 to 57% with an average value equal to 45% of the tensile strength of the GFRP straight bar. The reduced strength of the spirals could be attributed to localized stress concentration due to spiral curvature, spiral inclination, and the effect of the spiral stretching process. On the other hand, the test results indicate that the higher the GFRP spiral ratio, the lower the effective spiral stress. This is attributed to the reduction in the average spiral strain, which resulted from the distribution of the shear force on a larger number of spirals intersected by the diagonal shear cracks. Fig. 16 shows the CSA S806-12 stirrup stress and strain limits ($0.4f_{ftu}$ and $0.005E_v$, respectively) and the ACI 440.1R-15 strain limit ($0.004E_v$) compared to the effective spiral stress for all the specimens. The figure indicates that the $0.4f_{ftu}$ stress limit is closer to the average test results, and $0.005E_v$ provides the lower limit for the attained stress in the spirals. Therefore, the circular specimens design using CSA S806-12 resulted in failure governed by the $0.4f_{ftu}$ limit, and the capacity of the straight portions of the GFRP spirals could not be used. Consequently, using a value of less than $0.005E_v$ in design seems unnecessarily restrictive. This agrees well with the recommendation in the recent comparative study on the shear strength of FRP-RC members with stirrups (Razaqpur and Spadea 2015).

Beam Action versus Arch Action

Shear transfer mechanisms in reinforced concrete depend on the shear span-to-depth ratio. It has been well established that concrete beams with a rectangular cross section can be considered as slender or deep if a/d is greater or less than 2.0, respectively (ACI 318-14). This definition is not yet applicable to circular concrete members. Members with large a/d are dominated by beam action, in which the tension in the longitudinal reinforcement changes along the length of the beam. For such beams, shear is resisted by uncracked concrete in the compression zone, the interlocking action of aggregates, and the dowel action of the longitudinal reinforcement. For deep beams, however, after the breakdown of beam action, shear force is resisted mainly by arch action. In this mechanism, the longitudinal reinforcement has almost constant force from support to support, and the shear is carried by inclined struts (Kim and Park 1996; Mihaylov et al. 2010).

In this study, the a/d varied from 1.5 to 3. Fig. 17 shows the observed influence of a/d on the shear strength of the four tested beam specimens that had constant GFRP longitudinal ratio and spiral reinforcement ratio. This figure also provides the predicted strengths for these specimens, given the sectional models according to CSA S806-12, CSA S6-14, and ACI 440.1R-15 for specimens with $a/d \geq 2.0$. Moreover, CSA S806-12's strut-and-tie model was used to predict the shear strength of the tested specimens with $a/d \leq 2.0$. The details of these models will be discussed in the following section. The figure indicates that the experimental and predicted shear strength of the longer specimens was not significantly affected by a/d, whereas that of the shorter specimens increased greatly as a/d decreased. As is evident from Fig. 17, the beam with the a/d of 1.5 was 2.2 times stronger than the slender beam with the a/d of 2.6. Decreasing the a/d from 3 to 2.6 insignificantly increased the shear strength by 3%. For the specimens in the plot, the transition from strut to beam action occurred at the a/d greater than 2 and less than approximately 2.5. In this zone, the beam and arch action contributed to the overall shear resistance of the specimens. The test results indicated that a 21% enhancement in the shear strength was observed by decreasing a/d from 2.6 to 2.0 as a result of the contribution of arch action. Fig. 17 indicates that only CSA S806-12's sectional model accounts for this transition. This is attributed to the fact that CSA S806-12 includes a k_a to consider the V_{cf} by the arch effect for members with $a/d \leq 2.5$ (Appendix I). In contrast, ACI 440.1R-15 and CSA S6-14 sectional models do not account for this transition as shown in Fig. 17.

Theoretical Shear Strength

In this section, the available FRP shear design provisions for slender and deep flexural members are assessed for the nominal shear strength of the tested circular concrete specimens with shear span-to-depth ratios between 1.5 and 3. The sectional models and strut-and-tie model were applied to determine the expected V_r for the tested specimens with $a/d > 2.5$ and $a/d < 2.5$, respectively.

Sectional Models

For flexural members with $a/d > 2.5$, the FRP design codes and standards consider that a portion of the V_r, is carried by V_{cf}, with the remainder V_{sf} carried by truss mechanisms involving transverse reinforcement (the reinforcement contribution). To investigate the effect of the GFRP spiral reinforcement ratio on the design equation, the shear capacities of the tested specimens were assessed theoretically using the sectional models in ACI 440.1R-15, CSA S806-12, CSA S6-14, and JSCE (Appendix II). These models were developed based on the experimental work on the rectangular concrete members reinforced with FRP bars and bent FRP stirrups. Appendix I summarizes the shear design provisions of each code and design guideline. ACI 440.1R-15 and CSA S6-14 recommend that the effective strain in FRP shear reinforcement does not exceed 0.004, nor should the design strength exceed the strength of the bent portion of the stirrup (f_{fb}). The value of 0.004 is justified as the strain that prevents degradation of the aggregate interlock and the corresponding concrete shear (Priestley et al. 1994). ACI 440.1R-15, CSA S6-14, and JSCE provide design equations for the bend capacity of the FRP stirrup, which is a function of the ratio of the bend radius (r_b) to bar diameter (d_b). CSA S806-12 limits the maximum tensile stress in FRP shear reinforcement to be taken as the smaller of $0.005E_{fv}$, 40% of the ultimate longitudinal tensile strength of the FRP stirrup ($0.4f_{fu}$), or 1,200 MPa, irrespective of r_b/d_b. None of the previously mentioned codes or guidelines specifically address the assessment of circular elements reinforced with FRP spirals. The shear design parameters such as effective shear depth and width and the strength and strain limitation for FRP spirals are not defined. In the calculation, the approach proposed in *AASHTO LRFD Bridge Design Specifications* (AASHTO 2012) has been used to estimate the effective shear area of circular members, where the depth (d) was taken as equal to d [Eq. (2)], then $d_v = 0.9d$, and b_w was taken as the diameter of the circular cross section

$$d = \frac{D}{2} + \frac{D_r}{\pi} \tag{2}$$

Table 3 presents the statistical results related to the ratio between the experimental and the theoretical ultimate shear force (V_{exp}/V_{pred}). The average of V_{exp}/V_{pred} is directly related to accuracy. The analysis results indicate that the four methods investigated provided average ratios greater than 1.0. Table 3 indicates that V_{exp}/V_{pred} is higher for specimens with low shear reinforcement ratios than with high values. The CSA S806-12 method provided the closest predictions with a mean value equal to 1.61, followed by CSA S6-14 and ACI 440.1R-15 with mean values equal to 1.96 and 2.02, respectively. On the other hand, the JSCE method greatly underestimated the shear strength of the test specimens with an average V_{exp}/V_{pred} closer to 3.0. This excessive level of conservatism is relevant to the concept of calculating the FRP stirrup strain (ε_{fv}) at ultimate, which is limited to the lesser of the FRP stirrup bend strength or the value obtained from the JSCE strain design equation. This equation provides very low strain values at ultimate ranging between 0.0007 and 0.001 with an average value of 0.0009. On the other hand, the analysis results indicate that the ACI440.1R-15, CSA S6-14, and the JSCE design equations for bend strength are not appropriate for representing the strength of GFRP spirals. This was evident because these equations significantly overestimated the effective spiral stresses at failure. As mentioned previously, the $0.4f_{ftu}$ stress limit was closer to the average test results, and the $0.005E_v$ provides the lower limit for the attained stress in the spirals.

On the other hand, Table 3 confirms the unsuitability of the sectional models in predicting the nominal shear capacities for shear span-to-depth ratios less than 2.5, except for CSA S806-12, which conservatively predicted the strength of specimens with a/d of 2 and 1.5. As mentioned previously, this can be attributed to the included k_a that takes arch action into consideration.

Strut-and-Tie Model

Strut-and-tie modeling is a generalization of the truss analogy, in which a structural continuum is transformed into a discrete truss with compressive forces being resisted by the concrete and tensile forces by the reinforcement. The method is based on the lower bound theorem of plasticity providing capacity less than or equal to the structure's capacity. Over the last two decades, several researchers have conducted studies aimed at assessing the strength of concrete struts for use in strut-and-tie models. Generally, the

Table 3. Predicted Shear Strength of Test Specimens

Beam identifier	ACI 440.1R V_{exp}/V_{pred}	CSA S6-14 V_{exp}/V_{pred}	CSA S806-12 V_{exp}/V_{pred}	JSCE V_{exp}/V_{pred}	*Response-2000* V_{exp}/V_{pred}	Strut-and-tie model CSA S806-12 V_{exp}/V_{pred}	Proposed method V_{exp}/V_{pred}
B3.0-S0.35	1.99	1.9	1.74	2.88	1.17	—	—
B2.6-S0.26	2.23	2.1	1.58	2.79	1.01	—	—
B2.6-S0.35	2.06	2.0	1.60	2.97	1.03	—	—
B2.6-S0.53	1.82	1.8	1.55	3.35	1.18	—	—
Average	2.02	1.96	1.61	2.99	1.09	—	—
SD	0.17	0.12	0.08	0.25	0.09	—	—
COV	8.38	6.6	5.2	8.2	8.20	—	—
B2.0-0.35	2.50	2.4	1.60	3.60	0.99	1.69	1.32
B1.5-0.35	4.53	4.4	1.80	6.53	1.26	1.82	1.56
Average	3.51	3.4	1.70	5.06	1.12	1.75	1.44
SD	1.43	1.42	0.14	2.10	0.20	0.10	0.17
COV	40.8	41.6	8.30	40.9	17.0	5.24	11.8

Note: COV = coefficient of variation; SD = standard deviation.

approach has been to lump the effect of strut stress and strain conditions, reinforcement details, concrete strength, and uncertainties in the truss model into a single factor commonly referred to as the efficiency factor or, more recently, as the strength reduction factor for the concrete strut. ACI 318-14 (*Building Code Requirements for Structural Concrete and Commentary*) and bridge design specifications [*AASHTO LRFD Bridge Design Specifications* (AASHTO 2012)], adopted the use of strut-and-tie modeling in 2002 and 1994, respectively.

Based on the lower bound theory of plasticity, the capacity of an STM is always less than or equal to the capacity of the structure provided that (1) the truss model is in equilibrium, (2) sufficient deformation capacity exists to distribute forces within the assumed truss model, and (3) stresses applied to elements do not exceed their yield capacity. The yield capacity of a strut or node is equal to the effective compressive strength of the concrete within the strut or at the interface between the strut and node. A tie's yield capacity is equal to the lesser of the reinforcement tensile strength or the force that causes a loss of anchorage.

Although the application of the plasticity theory to materials of limited ductility, such as concrete, are limited in terms of plastic idealization, current STMs successfully predict the ultimate strength of concrete members reinforced with either steel or FRP bars (Andermatt and Lubell 2013a, b; Farghaly and Benmokrane 2014; Kim et al. 2014) by adopting the concept of the effective strength of concrete for a strut and node in the strut-and-tie model [Hong and Ha 2012; ACI 318-14; CSA S806-12; AASHTO LRFD (AASHTO 2012)]. The plastic distribution of stresses in the concrete requires that the tie is able to resist the concomitant tension and allow sufficient deformation for the plastic state of stress to develop in the concrete. In general, large deformations will not develop before the yielding of the steel bars. In the case of the GFRP bars, which can easily undergo a maximum strain from six to nine times greater than the steel's yield strain, the concrete can easily reach its plastic state before failure. In fact, the maximum strain in the GFRP tie may be larger than the maximum strain in the steel at failure. Consequently, the notion that the tie material experiences plastic deformation is not essential to satisfy the lower bound theorem of plasticity. Moreover, arch action was reported to be more efficient in the specimens reinforced with FRP than with steel. More bond slippage could occur with FRP reinforcement compared to steel because the FRP was sand-coated, producing a more efficient arch mechanism (El-Sayed 2006; Andermatt and Lubell 2010). Andermatt and Lubell (2013b) presented test data for 12 large-scale deep beams with internal FRP reinforcement that confirmed the presence of arch action. Then, a strut-and-tie modeling approach was developed for use in predicting the capacity of FRP-reinforced deep beams through mechanic-based modifications to existing STMs applicable to steel-reinforced concrete construction (Andermatt and Lubell 2013b). Recently, the strut-and-tie model was implemented in CSA S806-12 for designing FRP-RC members with low a/d values. This method is similar to the provisions in CSA A23.3-14 (CSA 2014b), CSA S6-14 (CSA 2014a), and *AASHTO LRFD Bridge Design Specifications* (AASHTO 2012) for steel reinforcement. A strength reduction factor ($v \leq 1.0$) for the strength of a concrete strut is introduced. Designing with the CSA S806-12 strut-and-tie model requires an orthogonal grid of reinforcing bars near each face for deep flexural members. For GFRP, the ratio of reinforcement area to gross concrete area shall not be less than 0.004 in each direction. The spacing of this reinforcement shall not exceed 200 mm for GFRP bars. If located within the tie, the crack control reinforcement may also be considered as tie reinforcement.

The strut-and-tie model of CSA S806-12 was used to predict the nominal shear strength for the two specimens that were tested with a/d of 1.5 and 2.0 (Appendix II). The ratio and spacing of GFRP orthogonal reinforcement (longitudinal and spiral) for both specimens are within the CSA S806-12's strut-and-tie design requirements (Clause 8.5.5: crack control reinforcement). The predicted capacity was based on the achieved stresses of (1) tensile stress of tie (longitudinal bars), (2) nodal stress at support and loading point, and (3) stress in the diagonal strut. An iterative process was conducted to determine the critical stress of the preceding three limit stresses. Once one of those three stresses was achieved, the assumed load was considered to be the predicted ultimate load capacity. So, the predicted loads are representing the lower bound solution (as the stresses on the other two items did not reach their limits). The lower bound theorem only requires the assumption of a statically admissible stress field and, in that sense, the conventional elastic analysis satisfies the lower bound theorem. In the case of the deep beams herein, the concrete stresses assumed to be in the nodal zones, the upper chord, and the diagonal struts will be achieved in GFRP-reinforced deep beams due to the large strain capacity of GFRP reinforcement. Finally, it is important to emphasize that CSA S806-12 assumes that the assumed plastic stress distribution in the case of the FRP-reinforced concrete deep beams can only be satisfied if failure is not initiated by the FRP tie (longitudinal reinforcement), and this is the case in the test results for the two beams with $a/d \leq 2$. Appendix I includes the strut-and-tie design equations from CSA S806-12. Moreover, Fig. 18 describes the strut-and-tie model using a simple idealization of the strut shape.

The analysis results indicate that the strut-and-tie model predictions (V_{STM}) are quite conservative for $a/d < 2.5$ with an average $V_{\text{exp}}/V_{\text{pred}}$ closer to 1.75. The high degree of conservatism does not justify the accuracy. This could be attributed to the fact that the CSA S806-12 strut-and-tie predictions do not consider the shear strength contributed by the shear reinforcement (GFRP spirals), whereas the observed failure modes of these specimens were a combination of strut crushing and rupture of GFRP spirals. The nominal capacities were re-estimated considering the GFRP spiral contribution using the CSA S806-12 design equation (Appendix I) as follows:

$$V_r = V_{\text{STM}} + V_{sf} \tag{3}$$

Table 3 presents the $V_{\text{exp}}/V_{\text{pred}}$ values for CSA S806-12 using the proposed design equation [Eq. (3)]. The proposed equation seems to give better predictions than the strut-and-tie equation. Table 3 indicates that $V_{\text{exp}}/V_{\text{pred}}$ is higher for specimens with

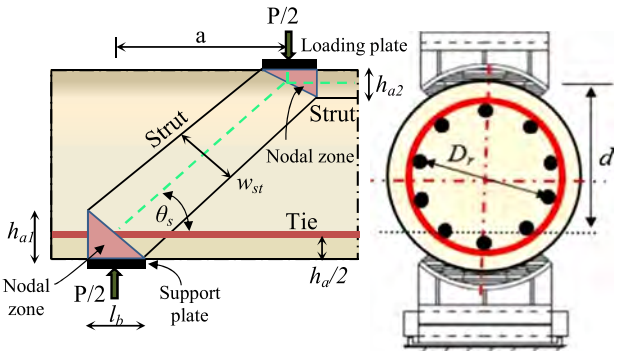

Fig. 18. Description of the strut-and-tie model using a simple idealization of the strut shape

low a/d ratios (1.5) rather than high (2). This modification yields a more reasonable estimate of the shear capacity and yet was conservative for both specimens tested in this investigation because the average experimental shear strength over the predicted value was 1.4 with a coefficient of variation of 11.8% and a standard deviation of 0.17 when using Eq. (3).

Shear Strength Predication Using the Modified Comparison Field Theory

A shear model based on the modified compression field theory was applied with *Response-2000 version 0.7.8* (R2K) software, which can be used to assess the shear strength of concrete cross sections with a wide range of geometries (Bentz 2000). *Response-2000* can make shear-strength predictions for sections that cannot be easily modeled with such traditional methods such as circular members and columns with spirals. Furthermore, it provides detailed output or results, including concrete and reinforcement stresses and strains, shear on cracks, concrete angle of principle compression, crack spacing at all layers, load deformation plots, and shear-moment interaction diagrams.

In this study, the full-member response method in *Response-2000* was implemented to predict the behavior of the tested circular members. When the FRP spiral reinforcement was defined in *Response-2000*, f_{fv} was defined as the governing spiral stress, which was taken as $0.4f_{fuv}$. Table 3 provides the comparison between the experimental and predicted values. The average value of $V_{\text{exp}}/V_{\text{pred}}$ for specimens with $a/d > 2.5$ is 1.09 with a standard deviation and a coefficient of variation equal to 0.09 and 8.2%, respectively. The corresponding values for specimens with $a/d < 2.5$ were 1.12, 0.2, and 17.0, respectively. The predicted shear strengths of the tested specimens are reasonably accurate but less conservative for the design issue.

Fig. 19 shows the predicted shear strain distribution along the shear span at the mid-depth of the cross section of the tested specimens. It can be seen that the average strain over the length of shear span is not uniform, and the strain increased linearly from the left (at support). The strain would be constant because the shear diagram is linear, but this was not the case due to concrete nonlinearity. The maximum shear strain at different a/d occurred at a distance from the support such as $0.5D$, $0.71D$, $0.96D$, and $1.34D$ for specimens B1.5-S0.35, B2.0-S0.35, B2.6-S0.35, and B3.0-S0.35, respectively. These distances are approximately close to the mid-shear span. In addition, the results of the modified comparison field theory (MCFT) analysis indicate that the higher shear strain occurred in B1.5-S0.35 and B2.0-S0.35. This can be attributed to tension developing in the compression chord due to the compression force in the strut. Fig. 19 also shows that B2.6-S0.26, with a lower shear reinforcement ratio, exhibited higher shear strain than the specimens with higher shear reinforcement (B2.6-S0.35 and B2.6-S0.53). This can be attributed to the fact that increasing the spiral reinforcement ratio constrained the cracked concrete core and enhanced the shear capacity by confining the concrete cross section.

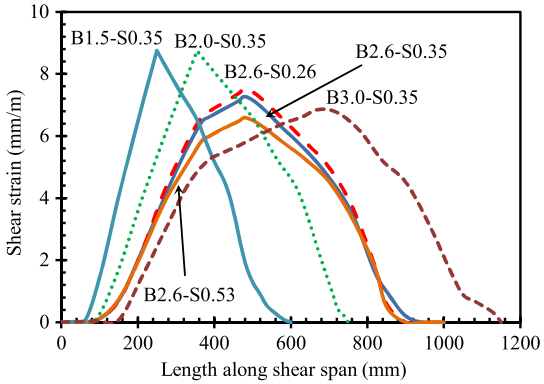

Fig. 19. Shear strain along the shear span by *Response-2000*

Conclusions

This paper presented tests that were performed to investigate the shear behavior of circular concrete members reinforced with GFRP bars and spirals. A total of six full-scale RC specimens were prepared to study the effect of the spiral reinforcement ratio and the shear span-to-depth ratio. Based on the experimental test results and analysis presented in this paper, the following conclusions can be drawn:

1. The mode of failure was mainly affected by the shear span-to-depth ratio, rather than the GFRP spiral reinforcement ratio; flexural-shear failure for specimens with $a/d = 3$, GFRP spiral rupture shear for specimens with $a/d = 2.6$, and strut crushing combined with spiral rupture for specimens with $a/d < 2.5$.
2. The shear strength of the GFRP-RC circular specimens with $a/d \leq 2.0$ was significantly dependent on arch action. In contrast, specimens with $a/d \geq 2.5$ were dominated by beam action and the effect of a/d was insignificant.
3. For GFRP-RC circular specimens, the transition from strut to beam action occurred at the a/d greater than 2 and less than approximately 2.5. In this zone, the beam and arch action contributed to the overall shear resistance of the beams.
4. The presence of GFRP spirals in the circular specimens enhanced the concrete contribution after the formation of the first shear crack. Moreover, increasing the spiral reinforcement ratio from 0.26 to 0.53% increased the shear resistance by 30.7% due to the spirals confining the concrete, which controls shear cracks and improves aggregate interlocking.
5. The results of this study indicate that the shear strength increased significantly with decreasing a/d ratio, where the shear strength increased by 21.4 and 120% with decreasing a/d by 25 and 42%, respectively.
6. While the sectional shear models in ACI 440.1R-15, CSA S806-12, CSA S6-14, and JSCE (1997) can be used to predict the shear strength of GFRP-RC circular specimens at $a/d > 2.5$, these equations provided overly conservative predictions. The CSA S806-12 model provided the most accurate predictions.
7. The test results reveal that the $0.4f_{fuv}$ spiral stress limit was closer to the test results for circular specimens and that $0.004E_{fv}$ or $0.005E_{fv}$ strain limit provides the lower limit for the attained stress in spirals.
8. The CSA S806-12 sectional model accounts for the transition in shear mechanism from beam to arch action for specimens with a $2.0 \leq a/d \leq 2.5$.
9. The CSA S806-12 strut-and-tie predictions underestimate the beneficial effect of adding GFRP spiral for circular specimens with the $a/d < 2.0$. A proposed modification was introduced to consider V_{sf} in the design equation.
10. *Response-2000* software, which is based on the MCFT, provided good predictions of the shear strength with an average value of $V_{\text{exp}}/V_{\text{pred}}$ equal to 1.09 and 1.12 for specimens with $a/d > 2.5$ and $a/d \leq 2.0$, respectively.

Appendix I. Shear Design Provisions

ACI 440.1R-15

$$V_{cf} = (2/5)k\sqrt{f'_c}b_w d \tag{4}$$

$$V_{sf} = (A_{fv}f_{fv}d/s)\sin\alpha \tag{5}$$

$$k = \sqrt{2\rho_f n_f + (\rho_f n_f)^2} - \rho_f n_f \tag{6}$$

$$f_{fv} = 0.004E_{fv} \le f_{fu\,\text{bent}} \tag{7}$$

$$f_{fu\,\text{bent}} = (0.05r_b/d_b + 0.3)f_{fu} \le f_{fu} \tag{8}$$

CSA S806-12

$$V_{cf} = 0.05\lambda\phi_c K_m K_r (f'_c)^{1/3} b_w d_v \tag{9}$$

$$V_{sf} = (\phi_f A_{fv} f_{fv} d_v/s)\cot\theta \tag{10}$$

$$V_r = V_{cf} + V_{sf} \le 0.22\phi_c f'_c b_w d_v \tag{11}$$

$$k_m = \sqrt{V_f \cdot d/M_f} \le 1.0 \tag{12}$$

$$k_r = 1 + (E_f\rho_f)^{1/3} \tag{13}$$

$$k_s = 750/(450 + d) \le 1.0 \tag{14}$$

$$2.5 \ge k_a = 2.5/(M_f/V_f d) \ge 1.0 \tag{15}$$

$$f_{fv} = 0.005E_f \le 0.4f_{fu} \tag{16}$$

$$\theta = 30 + 7{,}000\varepsilon_x \tag{17}$$

For d_v = geater value of $0.72D$ or $0.9d$

CSA S6-14

$$V_{cf} = 2.5\left[\frac{0.4}{(1 + 1{,}500\varepsilon_x)} \cdot \frac{1{,}300}{(1{,}000 + s_{ze})}\right] f_{cr} b_w d_v \tag{18}$$

$$V_{sf} = \phi_f A_{fv} f_{fv} d_v (\cot\theta + \cot\alpha)\sin\alpha/s \tag{19}$$

$$f_{fv} = 0.004E_{fv} \le f_{fu\,\text{bent}} \tag{20}$$

$$f_{fu\,\text{bent}} = (0.05r_b/d_b + 0.3)f_{fu}/1.5 \tag{21}$$

$$\varepsilon_x = \frac{(M_f/d_v) + V_f + 0.5N_f}{2(E_f A_f)} \le 0.003 \tag{22}$$

$$s_{ze} = 300 \text{ mm}$$

$$\theta = (30 + 7{,}000\varepsilon_x)\left(0.88 + \frac{s_{ze}}{2{,}500}\right) \tag{23}$$

For d_v = geater value of $0.72D$ or $0.9d$

JSCE (1997)

$$V_{cf} = \beta_d\beta_p\beta_n f_{vcd} b_w d/\gamma_b \tag{24}$$

$$V_{sf} = [A_{fv}E_{fv}\varepsilon_{fv}(\sin\alpha + \cos\alpha)/s]z/\gamma_b \tag{25}$$

$$\varepsilon_{fv} = 0.0001\sqrt{\left(\frac{h}{300}\right)^{-1/10} \cdot f'_{cd}\frac{\rho_f E_f}{\rho_{fv}E_{fv}}} \tag{26}$$

$$E_{fv}\varepsilon_{fv} \le f_{fu\,\text{bent}}$$

$$f_{fu\,\text{bent}} = (0.05r_b/d_b + 0.3)f_{fu}/1.3 \tag{27}$$

$$f_{vcd} = 0.2(f'_c)^{1/3} \le 0.72 \text{ N/mm}^2 \tag{28}$$

$$\beta_d = (1{,}000/d)^{1/4} \le 1.5 \tag{29}$$

$$\beta_p = (100\rho_f E_f/E_s)^{1/3} \le 1.5 \tag{30}$$

$$\beta_n = 1 + M_o/M_d \le 2 \quad \text{for } N'_d \ge 0 \tag{31}$$

$$\beta_n = 1 + 2M_o/M_d \ge 0 \quad \text{for } N'_d < 0 \tag{32}$$

Strut-and-tie model, CSA S806-12

$$f_{cu} = \nu f'_c \le 0.85f'_c \tag{33}$$

$$\text{Strut force} = \phi_c f_{cu} A_{cs} \tag{34}$$

$$\nu = 1/0.8 + 170\varepsilon_1 \tag{35}$$

$$\varepsilon_1 = \varepsilon_f + (\varepsilon_f + 0.002)\cot^2\theta_s \tag{36}$$

$$A_{cs} = W_{st} \cdot b \tag{37}$$

$$W_{st} = h_a\cos\theta_s + l_b\sin\theta_s \tag{38}$$

Appendix II. Shear Design Example (Beam B2.6-S0.35)

$f'_c = 49.5$ MPa, $E_f = 62.8$ GPa, $E_{fv} = 47$ GPa, $s = 150$ mm, $D = 500$ mm, $A_{fv} = 2 \times 127 = 254$ mm^2, $r_b = 210$ mm, $d_b = 12.7$ mm, $f_{fu} = 1{,}050$ MPa (shear reinforcement), $E_c = 31.63$ GPa, $\lambda = \emptyset_c = \emptyset_f = 1.0$

$$d = (D/2) + (D_r/\pi) = (500/2) + (397.3/3.14) = 377 \text{ mm}$$

ACI 440.1R-15

$$\rho_f = \frac{A_{frp}}{bxd} = \frac{5 \times 285}{500 \times 377} = 0.00756$$

$$n_f = \frac{E_f}{E_c} = \frac{62.8}{31.63} = 1.98$$

$$k = \sqrt{2\rho_f n_f + (\rho_f n_f)^2} - \rho_f n_f$$
$$= \sqrt{2(0.01497) + (0.01497)^2} - 0.01497 = 0.158$$

$$V_{cf} = (2/5)k\sqrt{f'_c}b_w d$$
$$= (2/5) \times 0.158 \times \sqrt{49.5} \times 500 \times 377/1{,}000 = 83.81 \text{ kN}$$

$$f_{fu\,\text{bent}} = (0.05 r_b/d_b + 0.3) f_{fu}$$
$$= (0.05 \times 210/12.7 + 0.3) \times 1{,}050 = 1{,}183 \text{ MPa} > f_{fu}$$
$$= 1{,}050 \text{ MPa}$$

Take $f_{fu\,\text{bent}} = f_{fu} = 1{,}050$ MPa

$$f_{fv} = 0.004 E_{fv} = 0.004 \times 47{,}000 = 188 \text{ MPa} \le f_{fu\,\text{bent}}$$

$$V_{sf} = (A_{fv} f_{fv} d/s) \sin\alpha = (254 \times 188 \times 377/150) \sin 80.3$$
$$= 118{,}265 \text{ N} = 118.3 \text{ kN}$$

$$V_{\text{pred}} = V_{cf} + V_{sf} = 83.81 + 118.27 = 202.1 \text{ kN}$$

CSA S806-12

$$k_m = \sqrt{V_f \cdot d/M_f} = \sqrt{d/a} = \sqrt{377/980} = 0.62 \le 1.0$$

$$k_r = 1 + (E_f \rho_f)^{1/3} = 1 + (62.8 \times 1000 \times 0.00756)^{1/3} = 8.80$$

For d_v = greater value of $0.72D$ or $0.9d = 360$ mm

$$A_{s\min} = 0.07\sqrt{f'_c}\frac{b_w s}{0.4 f_{fu}} = 392.9 \text{ mm}^2$$

$$k_s = 750/(450 + d) = 750/(450 + 377) = 0.907 \le 1.0$$

$$V_{cf} = 0.05 \lambda \phi_c K_m K_r (f'_c)^{1/3} b_w d_v K_s$$
$$= 0.05 \times 1 \times 1 \times 0.62 \times 8.80 \times (49.5)^{1/3}$$
$$\times 500 \times 360 \times 0.907/1000 = 163.7 \text{ kN}$$

$$0.22\sqrt{f'_c}b_w d_v = 291.77 \text{ kN} \ge V_{cf} \ge 0.11\sqrt{f'_c}b_w d_v = 146 \text{ kN ok}$$

$$V_{sf} = (\phi_f A_{fv} f_{fv} d_v/s)\cot\theta$$

$$f_{fv} = 0.005 E_{fv} = 0.005 \times 47{,}000 = 235 \text{ MPa} \le 0.4 f_{fu}$$

$$\varepsilon_x = \frac{V_f(a/d + 1)}{2E_f A_f} = 0.0037$$

$$\theta = 30 + 7{,}000\varepsilon_x = 30 + 7{,}000 \times 0.0037 = 55.9°$$

$$V_{sf} = (1 \times 254 \times 235 \times 360/150)\cot 55.9 = 97 \text{ kN}$$

$$V_{\text{pred}} = V_{cf} + V_{sf} = 163.7 + 96.99 = 261 \text{ kN}$$

CSA S6-14

$$V_{cf} = 2.5\left[\frac{0.4}{(1 + 1{,}500\varepsilon_x)} \cdot \frac{1{,}300}{(1{,}000 + s_{ze})}\right] f_{cr} b_w d_v$$

$$f_{cr} = 0.4\sqrt{49.5} = 2.84 \text{ MPa}$$

$$s_{ze} = 300 \text{ mm}$$

$$\varepsilon_x = \frac{V_f(a/d + 1)}{2E_f A_f} = 0.003$$

$$V_{cf} = 2.5\left[\frac{0.4}{(1 + 1{,}500 \times 0.003)} \cdot \frac{1300}{(1{,}000 + 300)}\right] 2.814$$
$$\times 500 \times 360/1{,}000 = 92.1 \text{ kN}$$

$$\theta = (30 + 7{,}000\varepsilon_x)(0.88 + s_{ze}/2{,}500)$$
$$= (30 + 7{,}000 \times 0.003)(0.88 + 300/2{,}500) = 50°$$

$$V_{sf} = \phi_f A_{fv} f_{fv} d_v (\cot\theta + \cot\alpha)\sin\alpha/s$$
$$= 1 \times 254 \times 188 \times 360(\cot 50 + \cot 80.3)\sin 80.3/150$$
$$= 114.3 \text{ MPa}$$

$$V_{\text{pred}} = V_{cf} + V_{sf} = 92.06 + 114.3 = 206 \text{ kN}$$

Acknowledgments

The authors would like to express their special thanks and gratitude to the Natural Science and Engineering Research Council of Canada (NSERC), NSERC and Industry Research Chair in Innovative FRP Reinforcement for Concrete Structures and the Fonds de la recherche du Quebec–Nature et Technologie (FRQ-NT) for their financial support and for the technical help provided by the staff of the structural lab of the Department of Civil Engineering at the University of Sherbrooke.

Notation

The following symbols are used in this paper:

A_{cs} = effective cross-sectional area of strut (mm^2);
A_f = total cross-sectional area of longitudinal tension reinforcement (mm^2);
A_{fv} = total cross-sectional area of spiral reinforcement (mm^2);
b_w = beam width (mm);
D = total diameter of circular member (mm);
D_r = diameter of the circle passing through the centers of the longitudinal reinforcement (mm);
d = effective depth of tensile reinforcement (mm);
d_b = bar diameter (mm);
d_v = effective shear depth (mm);
E_f = modulus of elasticity of FRP reinforcing bars (MPa);
E_{fv} = modulus of elasticity of FRP spirals (MPa);
E_s = modulus of elasticity of steel reinforcing bars (MPa);
f'_c = specified compressive strength of concrete (MPa);
f_{cr} = cracking strength of concrete (MPa);
f_{cu} = compressive stress in struts (MPa);
f_{fu} = tensile strength of straight portion of spirals (MPa);
$f_{fu\,\text{bent}}$ = strength of bent portion of FRP bar (MPa);
f_{fv} = stress in FRP spirals (MPa);
f'_{mcd} = design compressive strength of concrete allowing for size effect (MPa);
$k = \sqrt{2\rho_f n_f + (\rho_f n_f)^2} - \rho_f n_f$;
M_d = design bending moment (N · mm);
M_f = factored moment (N · mm);
M_o = decompression moment (N · mm);
N'_d = design axial force (N);

N_f = factored axial force (N);
n_f = ratio of modulus of elasticity of reinforcing bars to modulus of elasticity of concrete;
r_b = internal bend radius of the FRP spirals (mm);
S = spacing of spirals (mm);
S_{ze} = effective crack spacing for members without stirrups;
V_{cf} = FRP concrete shear strength (N);
V_{cr} = first diagonal shear crack (N);
V_{exp} = experimental shear strength (N);
V_f = factored shear load (N);
V_{pred} = predicted shear strength (N);
V_{sf} = spirals shear strength (N);
z = distance between points of action of tensile and compressive resultant forces; equal to $d/1.15$ (mm);
α = angle of inclination of the spiral (in degrees);
γ_b = safety factor (is taken as 1.3);
ε_f = tensile strain in the tie bar located closest to the tension face of the beam and inclined at θ_s to the strut;
ε_x = longitudinal strain at midheight of the cross section;
θ = angle of inclination of the principle diagonal compressive stress (in degrees);
θ_s = the smallest angle between the strut and the adjoining ties;
λ = factor accounting for concrete density;
λ_1 = effectiveness factor for circular section (is taken as 0.85);
λ_2 = factor accounting for spiral reinforcement (is taken as 1.0);
λ_3 = factor accounting for manufacturing of spirals (is taken 0.9);
ρ_f = FRP longitudinal reinforcement ratio;
ϕ_c = resistance factor for concrete; and
ϕ_f = resistance factor for FRP reinforcement.

References

AASHTO. (2012). *AASHTO LRFD bridge design guide specifications*, Washington, DC.

ACI (American Concrete Institute). (2004). "Guide test methods for fiber-reinforced polymers (FRPs) for reinforcing or strengthening concrete structures." *ACI 440.3R-04*, Farmington Hills, MI.

ACI (American Concrete Institute). (2014). "Building code requirements for structural concrete and commentary." *ACI 318-14*, Farmington Hills, MI.

ACI (American Concrete Institute). (2015). "Guide for the design and construction of structural concrete reinforced with fiber-reinforced polymer (FRP) bars." *ACI 440.1R-15*, Farmington Hills, MI.

Ahmed, E. A., El-Salakawy, E. F., and Benmokrane, B. (2010). "Performance evaluation of glass fiber-reinforced polymer shear reinforcement for concrete beams." *ACI Struct. J.*, 107(1), 53–62.

Alam, M., and Hussein, A. (2012). "Effect of member depth on shear strength of high-strength fiber-reinforced polymer-reinforced concrete beams." *J. Compos. Constr.*, 10.1061/(ASCE)CC.1943-5614.0000248, 119–126.

Alkhrdaji, T., Wideman, M., Belarbi, A., and Nanni, A. (2001). *Shear strength of RC beams and slabs*, J. Figueiras, L. Juvandes, and R. Faria, eds., A. A. Balkema Publishers, Netherlands, 409–414.

Andermatt, M. F., and Lubell, A. S. (2010). "Concrete deep beam reinforced with internal FRP." *Structural Engineering Rep. No. 291*, Dept. of Civil Engineering, Univ. of Alberta, Edmonton, AB, Canada.

Andermatt, M. F., and Lubell, A. S. (2013a). "Behavior of concrete deep beams reinforced with internal fiber-reinforced polymer—Experimental study." *ACI Struct. J.*, 110(4), 585–594.

Andermatt, M. F., and Lubell, A. S. (2013b). "Strength modeling of concrete deep beams reinforced with internal fiber-reinforced polymer." *ACI Struct. J.*, 110(4), 595–605.

Benmokrane, B., Ali, A. H., Mohamed, H. M., Robert, M., and ElSafty, A. (2016). "Durability performance and service life of CFCC tendons exposed to elevated temperature and alkaline environment." *J. Compos. Constr.*, 04015043.

Bentz, E. C. (2000). "Sectional analysis of reinforced concrete members." Ph.D. thesis, Dept. of Civil Engineering, Univ. of Toronto, Toronto.

Bentz, E. C., Massam, L., and Collins, M. P. (2010). "Shear strength of large concrete members with FRP reinforcement." *J. Compos. Constr.*, 10.1061/(ASCE)CC.1943-5614.0000108, 637–646.

BP Composites. (2014). "Product technical specifications." Edmonton, AB, Canada.

Clarke, J. L., and Birjandi, F. K. (1993). "The behaviour of reinforced concrete circular section in shear." *J. Struct. Eng.*, 71(5), 73–78, 81.

Collins, M. P., Bentz, E. C., and Sherwood, E. G. (2008). "Where is shear reinforcement required? A review of research results and design procedures." *ACI Struct. J.*, 105(6), 590–600.

Collins, M. P., Bentz, E. C., Sherwood, E. G., and Xie, L. (2007). "An adequate theory for the shear strength of reinforced concrete structures." *Morley Symp. on Concrete Plasticity and its Applications*, Univ. of Cambridge, Cambridge, U.K., 75–93.

CSA. (Canadian Standards Association). (2010). "Specification for fibre-reinforced polymers." *CAN/CSA S807-10*, Rexdale, ON, Canada.

CSA. (Canadian Standards Association). (2012). "Design and construction of building components with fibre-reinforced polymers." *CAN/CSA S806-12*, Rexdale, ON, Canada.

CSA. (Canadian Standards Association). (2014a). "Canadian highway bridge design code." *CAN/CSA S6-14*, Rexdale, ON, Canada.

CSA. (Canadian Standards Association). (2014b). "Design of concrete structures for buildings." *CAN/CSA A23.3-04*, Rexdale, ON, Canada.

El-Sayed, A. K. (2006). "Concrete contribution to the shear resistance of FRP-reinforced concrete beams." Ph.D. dissertation, Univ. de Sherbrooke, QC, Canada.

El-Sayed, A. K., and Benmokrane, B. (2008). "Evaluation of the new Canadian highway bridge design code shear provisions for concrete beams with fiber-reinforced polymer reinforcement." *Can. J. Civ. Eng.*, 35(6), 609–623.

El-Sayed, A. K., El-Salakawy, E. F., and Benmokrane, B. (2006). "Shear strength of FRP-reinforced concrete beams without transverse reinforcement." *ACI Struct. J.*, 103(2), 235–243.

Farghaly, A., and Benmokrane, B. (2014). "Shear behavior of FRP-reinforced concrete deep beams without web reinforcement." *J. Compos. Constr.*, 10.1061/(ASCE)CC.1943-5614.0000385, 04013015.

Felthem, I. (2004). "Shear in reinforced concrete piles and circular columns." *Struct. Eng.*, 82(11), 27–31.

Fico, R., Prota, A., and Manfredi, G., (2008). "Assessment of eurocode-like design equations for the shear capacity of FRP RC members." *Compos. Eng. Part B*, 39(5), 792–806.

Guadagnini, M., Pilakoutas, K., and Waldron, P. (2006). "Shear resistance of FRP RC beams: Experimental study." *J. Compos. Constr.*, 10.1061/(ASCE)1090-0268(2006)10:6(464), 464–473.

Hong, S., and Ha, T. (2012). "Effective capacity of diagonal strut for shear strength of reinforced concrete beams without shear reinforcement." *ACI Struct. J.*, 109(2), 139–148.

Ishihara, K., Obara, T., Sato, Y., Ueda, T., and Kakuta, Y. (1997). "Evaluation of ultimate strength of FRP rods at bent-up portion." *Proc., 3rd Int. Symp. on Nonmetallic (FRP) Reinforcement for Concrete Structures*, Vol. 2, Japan Concrete Institute (JCI), Sapporo, Japan, 27–34.

Jensen, U. G., Hoang, L. C., Joergensen, H. B., and Fabrin, L. S. (2010). "Shear strength of heavily reinforced concrete members with circular cross section." *J. Eng. Struct.*, 32(3), 617–626.

JSCE (Japan Society of Civil Engineers). (1997). "Recommendation for design and construction of concrete structures using continuous fiber reinforcing materials." Tokyo.

Kani, M. W., Huggins, M. W., and Wittkopp, R. R. (1979). *Kani on shear in reinforced concrete*, University of Toronto Press, Toronto.

Khalifa, J. U., and Collins, M. P. (1981). "Circular reinforced concrete members subjected to shear." Dept. of Civil Engineering, Univ. of Toronto, Toronto.

Kim, D. J., Lee, J., and Lee, Y. H. (2014). "Effectiveness factor of strut-and-tie model for concrete deep beams reinforced with FRP rebars." *Compos. Part B*, 56, 117–125.

Kim, J. K., and Park, Y. D. (1996). "Prediction of shear strength of reinforced concrete beams without web reinforcement." *ACI Mater. J.*, 93(3), 213–222.

Merta, I., and Kolbitsch, A. (2006). "Shear area of RC circular cross section members." *31st Conf. on our World in Concrete and Structures*, Concrete Institute, CI-Premier, Singapore.

Mihaylov, B. I., Bentz, E. C., and Collins, M. P. (2010). "Behavior of large deep beams subjected to monotonic and reversed cyclic shear." *ACI Struct. J.*, 107(6), 726–734.

Mohamed, H. M., Afifi, M. Z., and Benmokrane, B. (2014). "Performance evaluation of concrete columns reinforced longitudinally with FRP bars and confined with FRP hoops and spirals under axial load." *J. Bridge Eng.*, 10.1061/(ASCE)BE.1943-5592.0000590, 04014020.

Mohamed, H. M., and Benmokrane, B. (2014). "Design and performance of reinforced concrete water chlorination tank totally reinforced with GFRP bars: Case study." *J. Compos. Constr.*, 10.1061/(ASCE)CC.1943-5614.0000429, 05013001.

Nanni, A., and Faza, S. (2002). "Designing and constructing with FRP bars: An emerging technology." *ACI Concr. Int.*, 24(11), 53–58.

Priestley, M. J. N., Verma, R., and Xiao, Y. (1994). "Seismic shear strength of reinforced concrete columns." *J. Struct. Eng.*, 10.1061/(ASCE)0733-9445(1994)120:8(2310), 2310–2329.

Razaqpur, A., and Spadea, S. (2015). "Shear strength of FRP reinforced concrete members with stirrups." *J. Compos. Constr.*, 10.1061/(ASCE)CC.1943-5614.0000483, 04014025.

Response-2000 version 0.7.8 [Computer software]. Univ. of Toronto, Toronto, ⟨http://www.ecf.utoronto.ca/~bentz/r2k.htm⟩.

Shehata, E., Morphy, R., and Rizkalla, S. (2000). "Fibre reinforced polymer shear reinforcement for concrete members: Behaviour and design guidelines." *Can. J. Civ. Eng.*, 27(5), 859–872.

Sherwood, E. G., and Noghreh Khaja, M. (2012). "The strain effect in FRP-reinforced structures." *6th Conf. in Advanced Composite Materials in Bridges and Structures (ACMBS-VI)*, ISIS Canada Network Association, Queen's Univ., Kingston, ON, Canada.

Thomas, J., and Ramadass, S. (2015). "Design for shear strength of concrete beams longitudinally reinforced with GFRP bars." *Struct. Eng. Mech.*, 53(1), 41–55.

Tottori, S., and Wakui, H. (1993). "Shear capacity of RC and PC beams using FRP reinforcement." *ACI Struct. J.*, 138, 615–632.

Turmo, J., Ramos, G., and Aparicio, A. C. (2009). "Shear truss analogy for concrete members of solid and hollow circular cross section." *J. Eng. Struct.*, 31(2), 455–465.